Electronic Supplementary Material (ESI) for Journal of Materials Chemistry A.
This journal is © The Royal Society of Chemistry 2023

Supplementary Information

PTFE Nanocoating on Cu Nanoparticles through Dry Processing to Enhance Electrochemical Conversion of CO_2 towards Multi-Carbon Products

John Pellessier,‡ Xiangtao Gong,‡ Boyang Li, Jiaqi Zhang, Yang Gang, Kirk Hambleton, Chinmoy Podder, Zhongjia Gao, Hongcai Zhou, Guofeng Wang, Heng Pan* and Ying Li *

J. Pellessier, X. Gong, Y. Gang, K. Hambleton, C. Podder, Z. Gao, H.Pan, Y. Li
J. Mike Walker ‘66 Department of Mechanical Engineering
Texas A&M University
College Station, Texas 77843, USA.
Email: *yingli@tamu.edu, hpan@tamu.edu*

B. Li, G. Wang
Department of Mechanical Engineering and Materials Science
University of Pittsburgh
Pittsburgh, PA 15261, USA

J. Zhang, H Zhou
Department of Chemistry
Texas A&M University
College Station, Texas 77843, USA.

‡These authors contributed equally.

*Corresponding authors.

Methods:

Distinguishing Cu NPs and PTFE NPs under SEM:

In this study, SEM observations of Cu NPs and PTFE NPs were used to investigate the Cu PTFE interaction. Fig. S1a shows two clusters of Cu NPs and PTFE NPs respectively. In general, the PTFE NPs have larger size than that of Cu NPs, however some of the smaller PTFE NPs are in the same size range of Cu NPs, and the PTFE can deform after granulation, so it is not reliable to distinguish between Cu and PTFE nanoparticles just by the size. The zoom-in images of Cu and PTFE NPs show that the Cu and PTFE have very different textured surfaces, the Cu NPs have smaller grains while the PTFE have the crack-like surface texture, so it is more reliable to distinguish between them by its texture after granulation.

Electrochemical CO_2RR Activity Measurements:

All electrochemical tests were performed in a three-electrode flow cell electrolyzer, a schematic of the flow cell is shown in Fig. S13. An anion exchange membrane (AEM, Fumasep PK 130, Fuel Cell Stores) was used to separate the cathode and anode chambers of the flow cell and prevent product cross over. Nickel foam was used as the anode. The cathode and anode were both loaded to have a working area of 1 cm^2. A Hg/HgO electrode (1 M KOH) was used as the reference electrode. 1 M KOH was circulated separately in the cathode and anode chambers. High purity CO_2 (Airgas, 99.999%) was continually supplied to the back of the cathode at a flow rate of ~30 mL min^{-1}, where it could diffuse into the GDL and react with the catalyst and electrolyte interface. A constant current was applied to the cell via a DC power supply (Agilent E3633A), and the potential between the working and reference electrodes was measured by a multimeter (AidoTek VC97+).[1-3] Applied potentials were converted to the reversible hydrogen electrode (RHE) scale based on Equation s1,

$$E\ (versus\ RHE) = E\ (versus\ Hg/HgO)\ +0.098\ +0.0591\ x\ pH \tag{S1}$$

where the pH for 1 M KOH was 14. Solution resistance was accounted for by performing iR correction utilizing electrochemical impedance spectroscopy (EIS) performed at open circuit voltage (OCV).[4, 5]

Product selectivity calculation:

Gas phase products we analyzed directly from the cathode chamber via an online gas chromatograph (GC, GC-2010, Shimadzu) equipped with a thermal conductivity detector (TCD) to analyze CO and H_2 and flame ionization detector (FID) to analyze CH4 and C2H4. Gas products were analyzed two times for each cathode and applied current density. Liquid products from the cathode electrolyte were analyzed after electrochemical testing by NMR (1H NMR, Bruker 400 MHz spectrometer). The faradaic efficiency for gas and liquid products, respectively, were calculated using Equation s2 and s3,

$$FE = \frac{zPFC_i v}{jRT} \tag{S2}$$

$$FE = \frac{zFC_i V}{Q} \tag{S3}$$

where z is the number of electrons transferred per molecule of the target product i, P is the pressure (101 kPa), F is Faraday's constant (96,500 C mol^{-1}), C_i is the volume concentration of the target products determined by GC or NMR, v is the flow rate of CO_2 supplied to the back of the cathode, j is the steady-state current applied to the cathode, R is the universal gas constant (8.314 J mol^{-1} K^{-1}), T is the temperature (298.15 K), V is the total volume of electrolyte collected then tested, and Q is the total charge supplied to the cell during testing.

Computational Details:

The first-principles density functional theory (DFT)[6, 7] calculations with plane wave basis set were performed using the Vienna ab initio simulation package (VASP) software[8, 9]. The core electrons were described using the projector augmented wave (PAW)[10, 11] pseudopotential. The cut-off energy of plane wave basis set was set as 500 eV to expand the wave functions. The generalized gradient approximation (GGA) of the revised Perdew, Burke and Ernzernhof (RPBE)[12] functionals was used to describe the electronic exchange and correlation energy term. The lattice parameter of bulk Cu was optimized to be 3.67 Å and the length of PTFE along the chain direction was relaxed to be 1.24 Å per unit CF_2. The Cu(111) surface model consists of 4 layers with each layer containing 12 Cu atoms and the Cu(100) surface model consists of 5 layers with each layer containing 9 Cu atoms. In addition, a 14 Å vacuum region was added perpendicularly to the modelled Cu surfaces to separate periodic images. The Brillouin zone was sampled by Monkhorst-pack[13] 6×6×1 k-point grid for Cu(100) and 5×5×1 k-point grid for Cu(111), respectively.

During structural optimization, the top two atomic layers in Cu(100) and Cu(111) model together with adsorbates were allowed to relax until the force on each ion fell below 0.02 eV/Å. The free energy of a chemical reaction was calculated as follows in Equation S4,

$$\Delta G = \Delta E_{DFT} + \Delta E_{ZPE} + \Delta H_T - T\Delta S \tag{S4}$$

where ΔE_{ZPE} is the energy change derived from DFT calculation, ΔE_{ZPE} is the zero-point energy change, ΔH_T is the enthalpy change from 0 K to T K, and ΔS is entropy change for the reaction. ZPE corrections were calculated as ZPE $= \sum \frac{1}{2} h v_i$, where h is the Planck's constant and v_i is the frequency of the corresponding vibrational mode of binding molecules. The vibrational heat capacity integration $\int_0^T C_p(t)dt$ was used to calculate the ΔH_T. The entropy term is calculated as in Equation S5,

$$S = k_B * \sum_i \left(\frac{hv_i}{k_BT} * \frac{1}{\exp\left(\frac{hv_i}{k_BT}\right) - 1} - \ln\left[1 - \exp\left(-\frac{hv_i}{k_BT}\right)\right] \right) . \tag{S5}$$

Where, T is the temperature of reaction, S is the vibrational entropy, h is the Planck's constant, k_B is the Boltzmann constant, v_i is the frequency of the i^{th} vibrational mode.

Here, we adopted the pathway of CO_2 reduction to C_{2+} products proposed by Koper.[14, 15] The CO_2 reduction to C_{2+} products will start from the adsorption of CO_2 molecules on Cu surface. The adsorbed CO_2 will first be hydrogenated to form *COOH which will dissociate to form *CO. Subsequently, two adsorbed *CO could dimerize to form *COCO through a CO-CO coupling process, and then the adsorbed *COCO will be protonated to form *COCHO. Alternatively, the adsorbed CO could be first hydrogenated to form *CHO which will then be coupled with another CO to form *COCHO via a CO-CHO coupling process. Moreover, the adsorbed *COCHO will be protonated to form *CCO, *CHCO, *CHCHO, and *CH_2CHO, sequentially. Toward selectively producing ethylene, *CH_2CHO will be further protonated to form *O+C_2H_4(g) and finally H_2O+C_2H_4(g). In contrast, toward producing ethanol, *CH_2CHO will be further protonated to form *CH_3CHO, and CH_3CH_2OH(l). The selectivity toward a specific two-carbon (C_2) product (i.e., ethylene or ethanol) on Cu is determined by the free energy changes for the different protonation steps of *CH_2CHO.

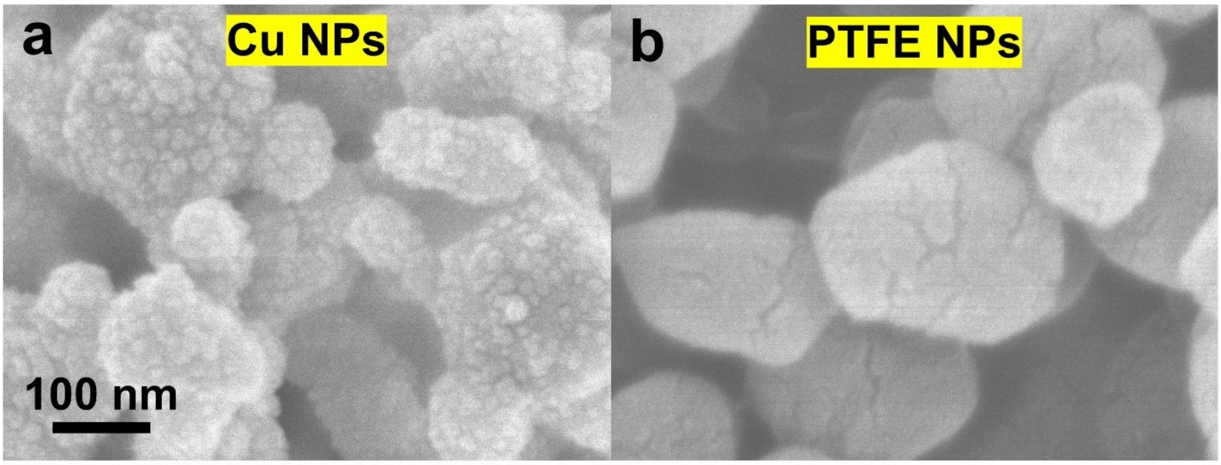

Fig. S1. SEM images showing clusters of (a) Cu nanoparticles and (b) PTFE nanoparticles.

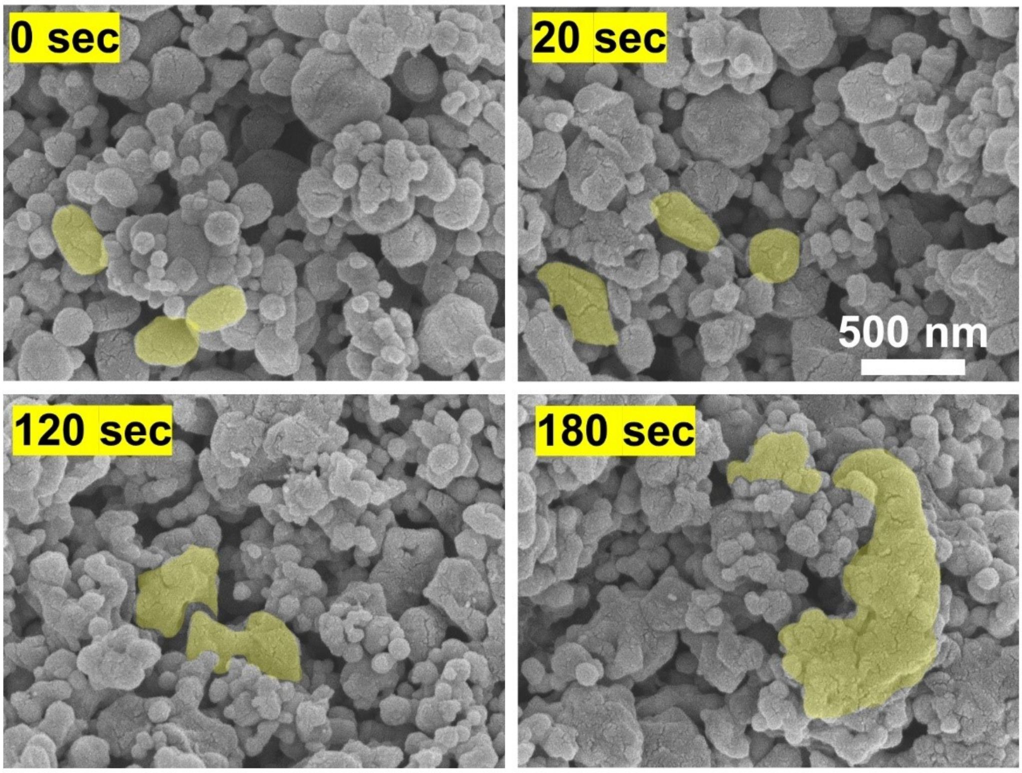

Fig. S2. SEM for Cu and PTFE at different ball-milling time, some of the PTFE is highlighted in yellow for better viewing.

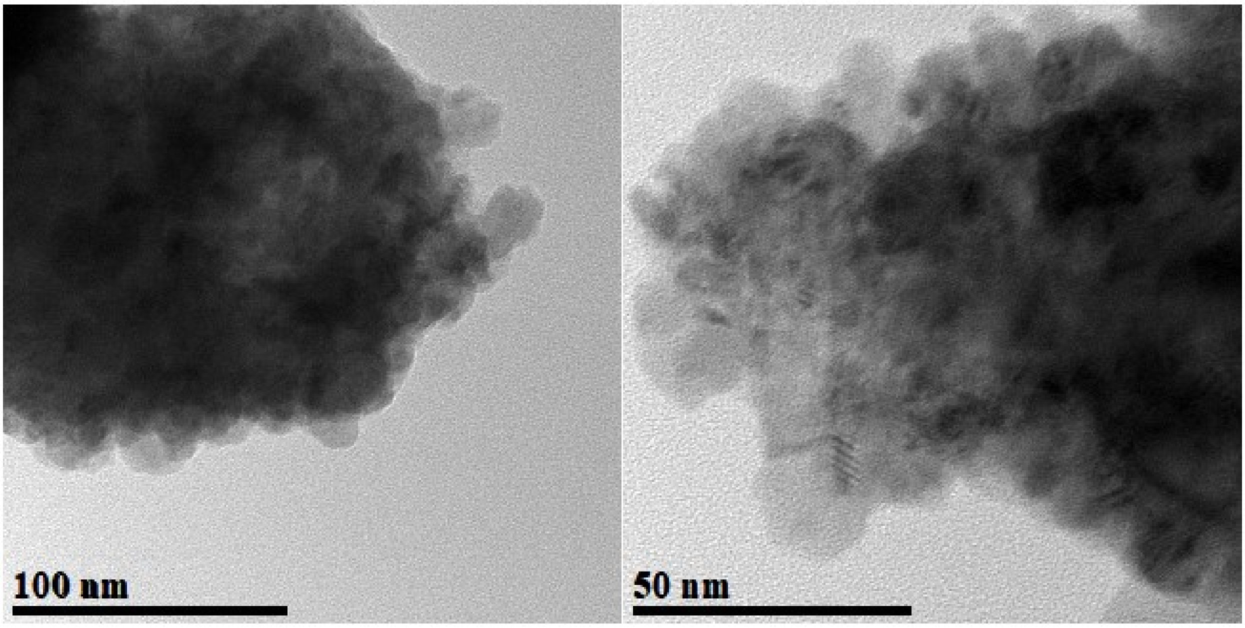

Fig. S3. TEM images of WET/20%PTFE catalyst powder.

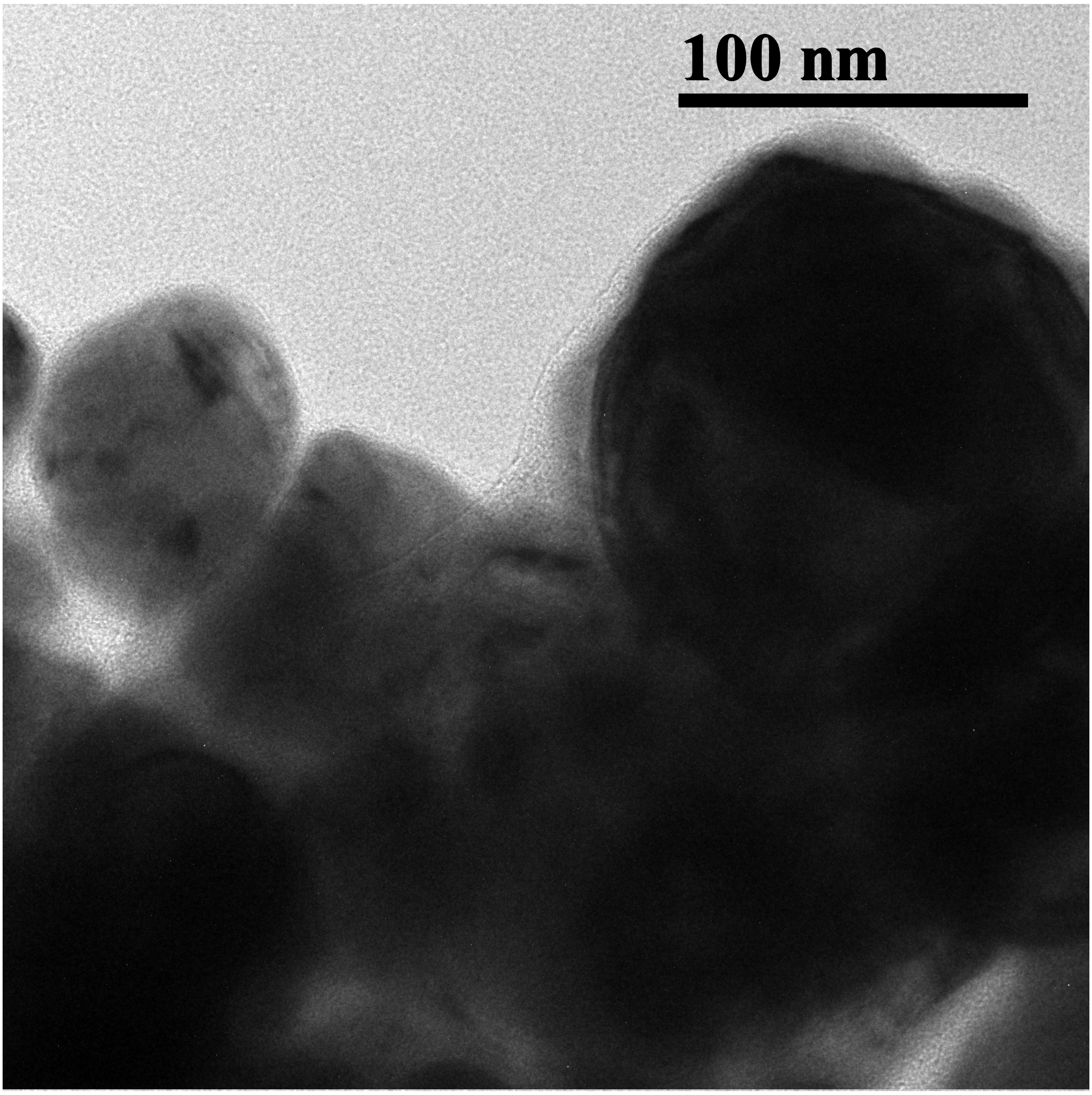

Fig. S4. Additional TEM image of DRY/20%PTFE/30min catalyst powder.

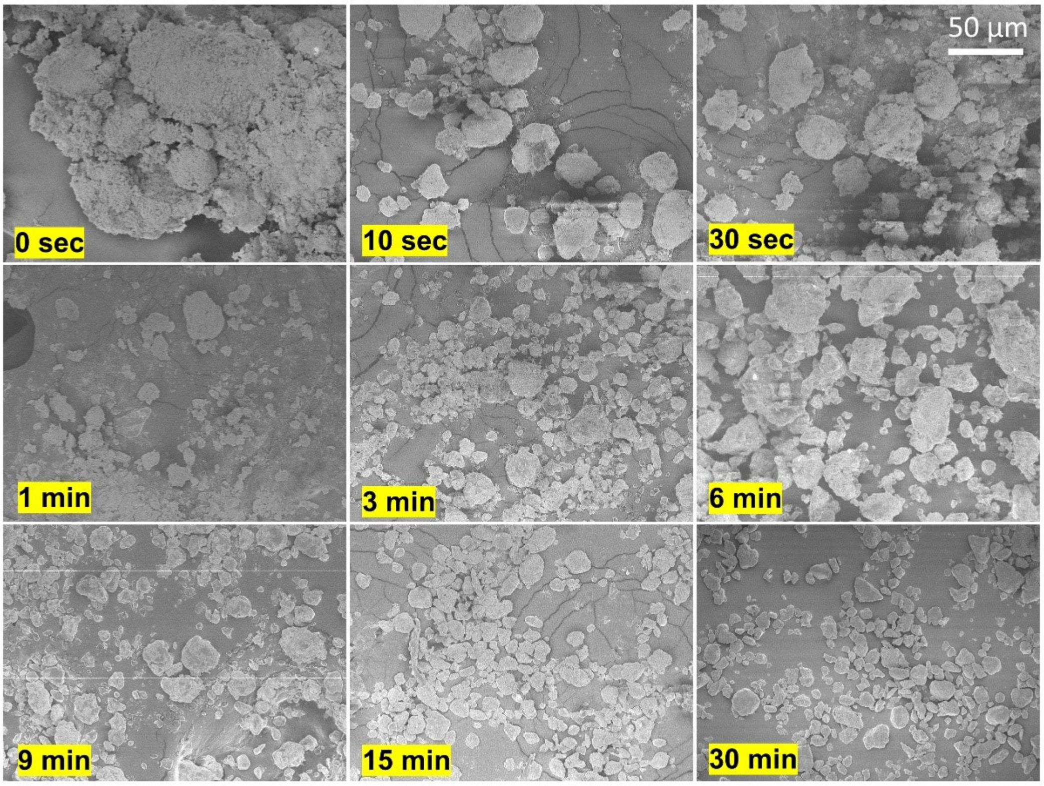

Fig. S5. SEM images showcasing the effect varying the granulation time has on the morphology of the resulting catalyst. All samples shown here were prepared using 80% Cu and 20% PTFE.

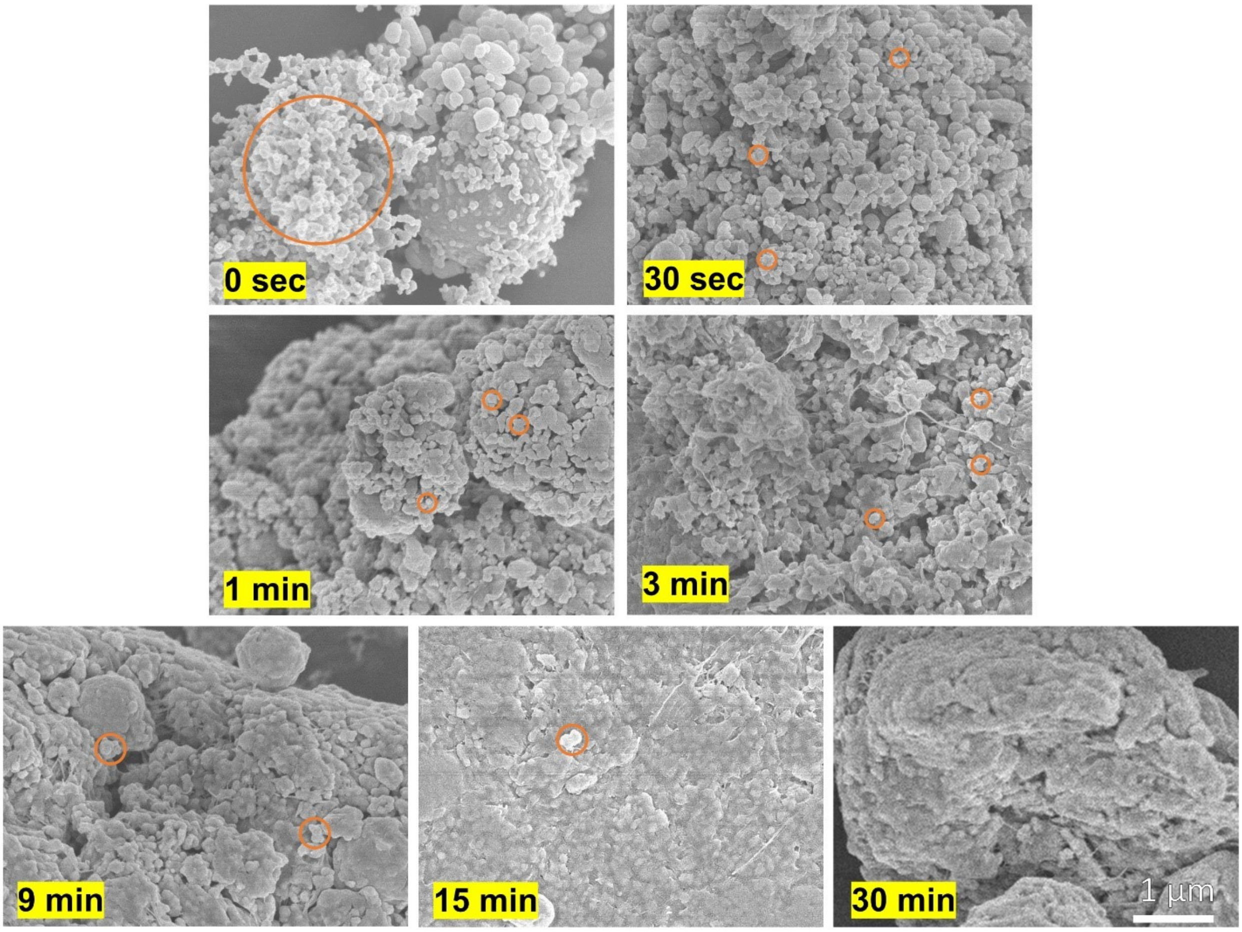

Fig. S6. SEM images showcasing the effect varying the granulation time has on the surface morphology of the resulting catalyst. Also showcasing the deformation of the PTFE NP over time. All samples shown here were prepared using 80% Cu and 20% PTFE. Orange Circles highlight examples of fully exposed Cu NPs.

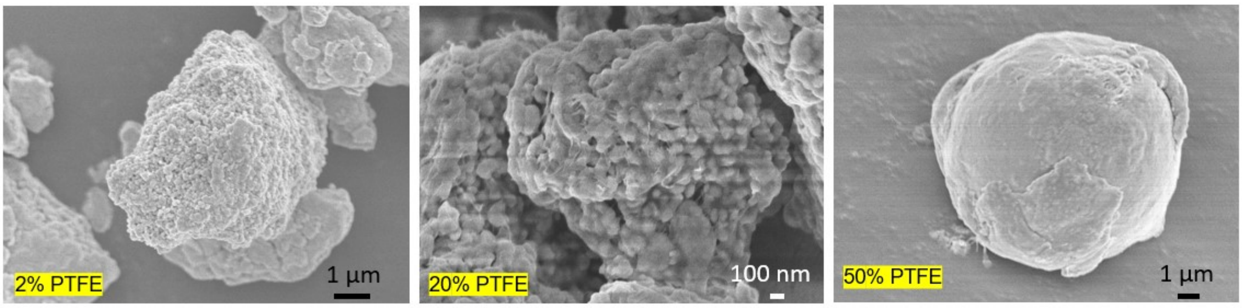

Fig. S7. SEM images showcasing the effect varying the PTFE mass loading has on the morphology of the resulting catalyst. All samples shown here were prepared using a ball-milling time of 30 min.

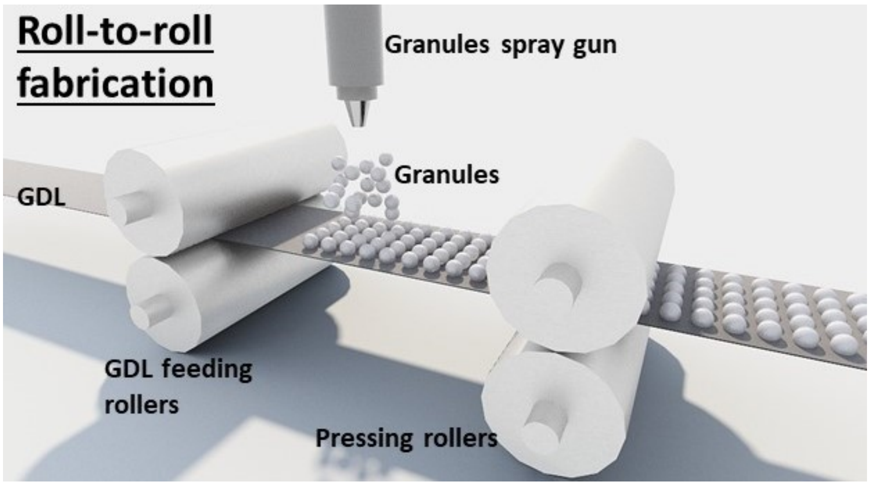

Fig. S8. Schematic illustration of Roll-to-Roll fabrication for the innovative cathode

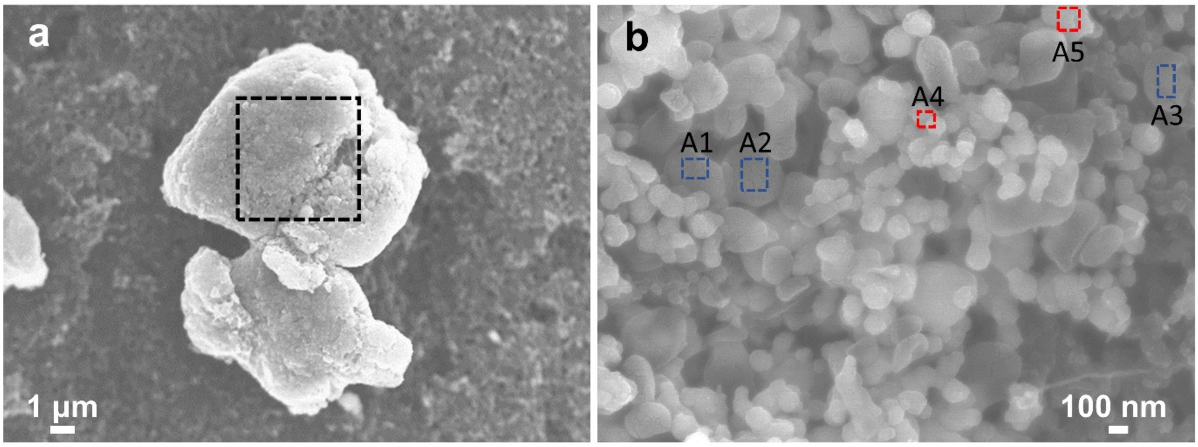

Fig. S9. SEM images and EDS analyses of prepared catalysts: (a) DRY/20%PTFE/30min, (b) WET/20%PTFE. EDS analyses indicate that on DRY/20%PTFE/30min the weight ratio of Cu to F is 3.35, and on WET/20%PTFE the areas of A1, A2, and A3 contain 100% F but no Cu, while A4 and A5 contain 100% Cu but no F.

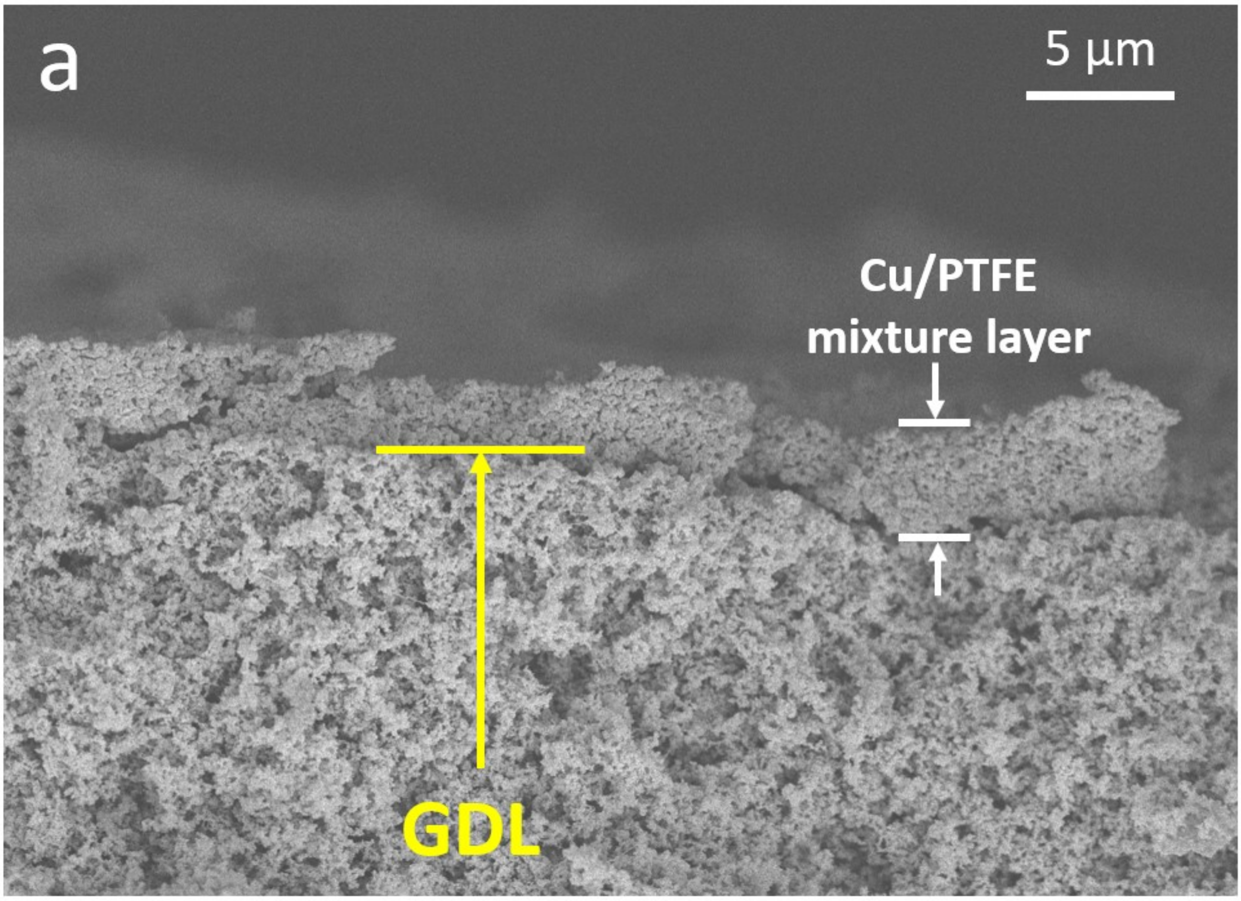

Fig. S10. SEM image of the cross section of a prepared WET/20%PTFE cathode.

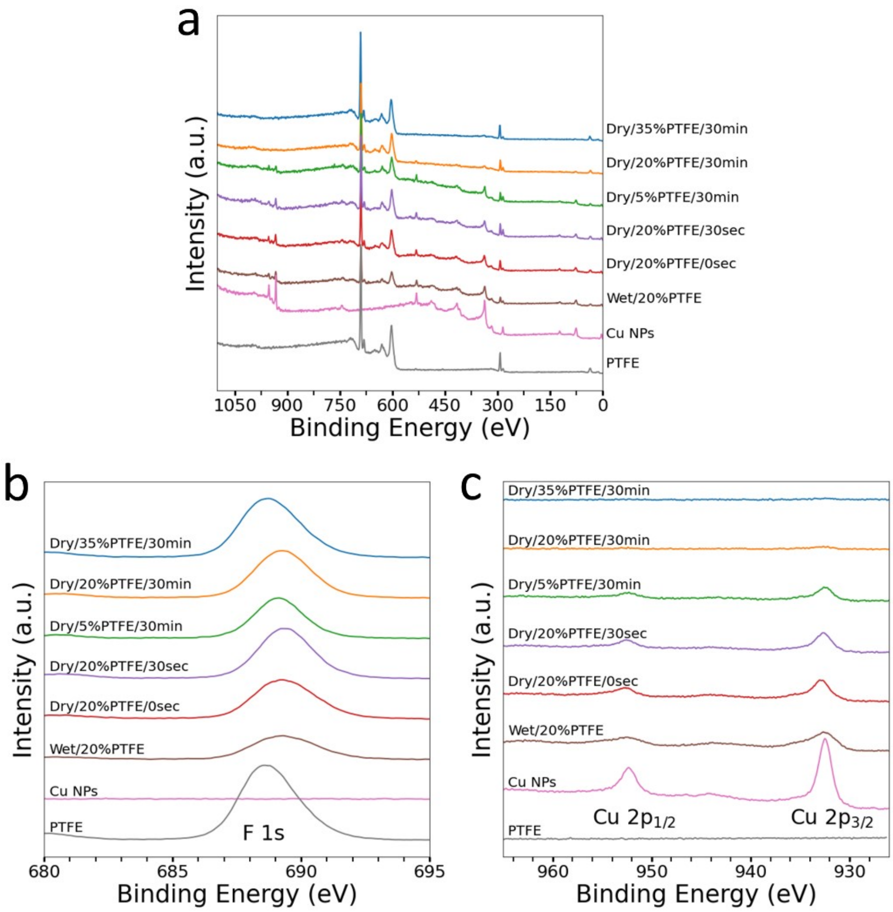

Fig. S11. (a) Full range XPS and High resolution XPS analysis of (b) F 1s and (c) Cu 2p peaks for select catalyst powders.

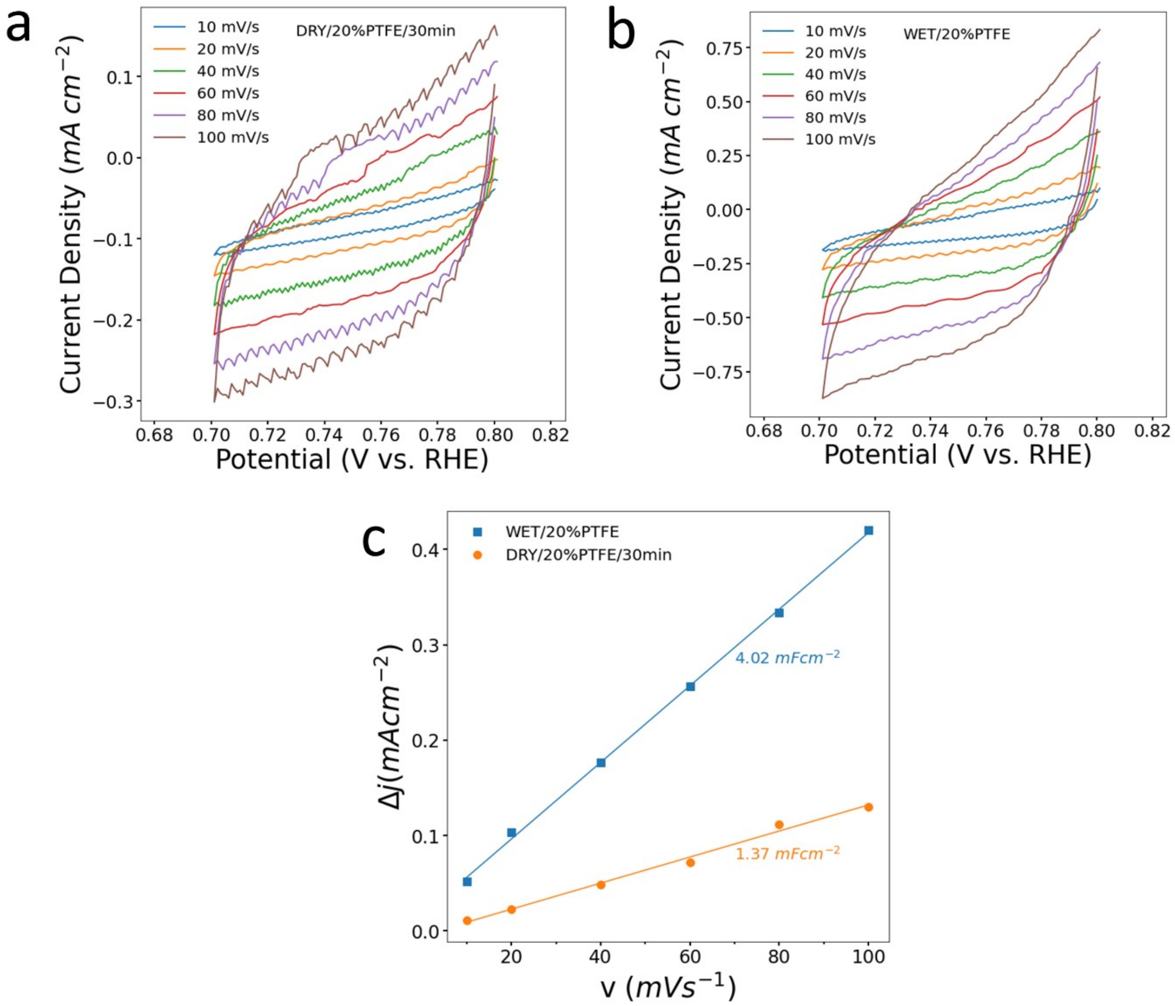

Fig. S12. Cyclic voltammograms of (a) DRY/20%PTFE/30min and (b) WET/20%PTFE under various scan rates. (c) Current density plotted against CV scan rates for DRY/20%PTFE/30min and WET/20%PTFE to find the double-layer capacitance.

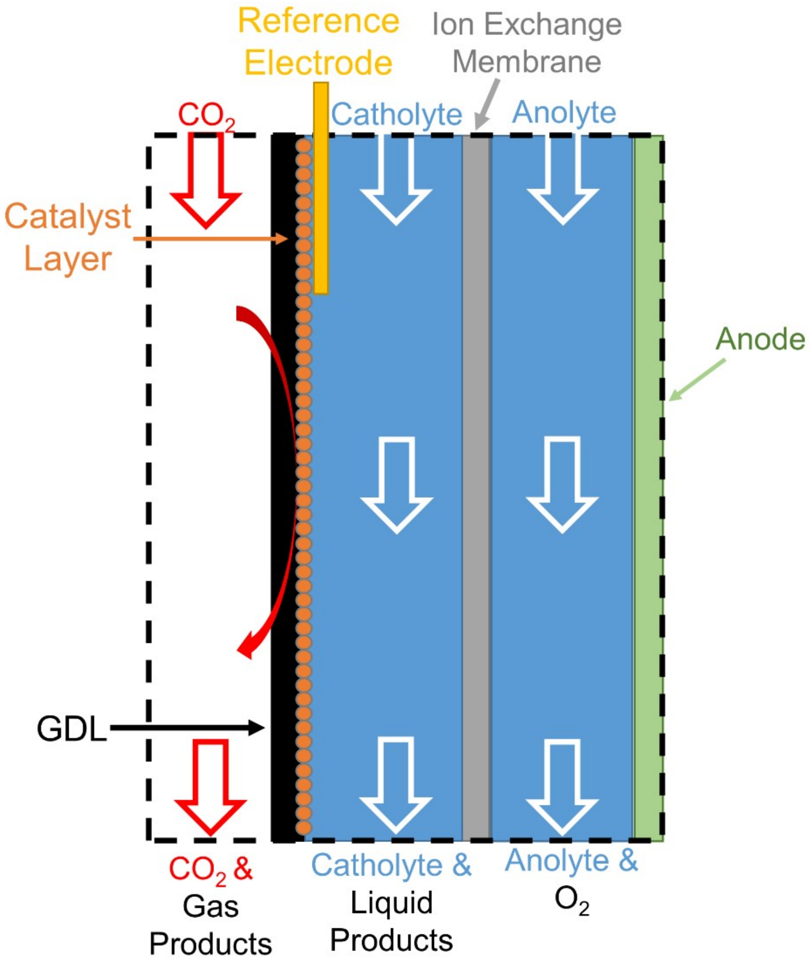

Fig. S13. Schematic of flow cell.

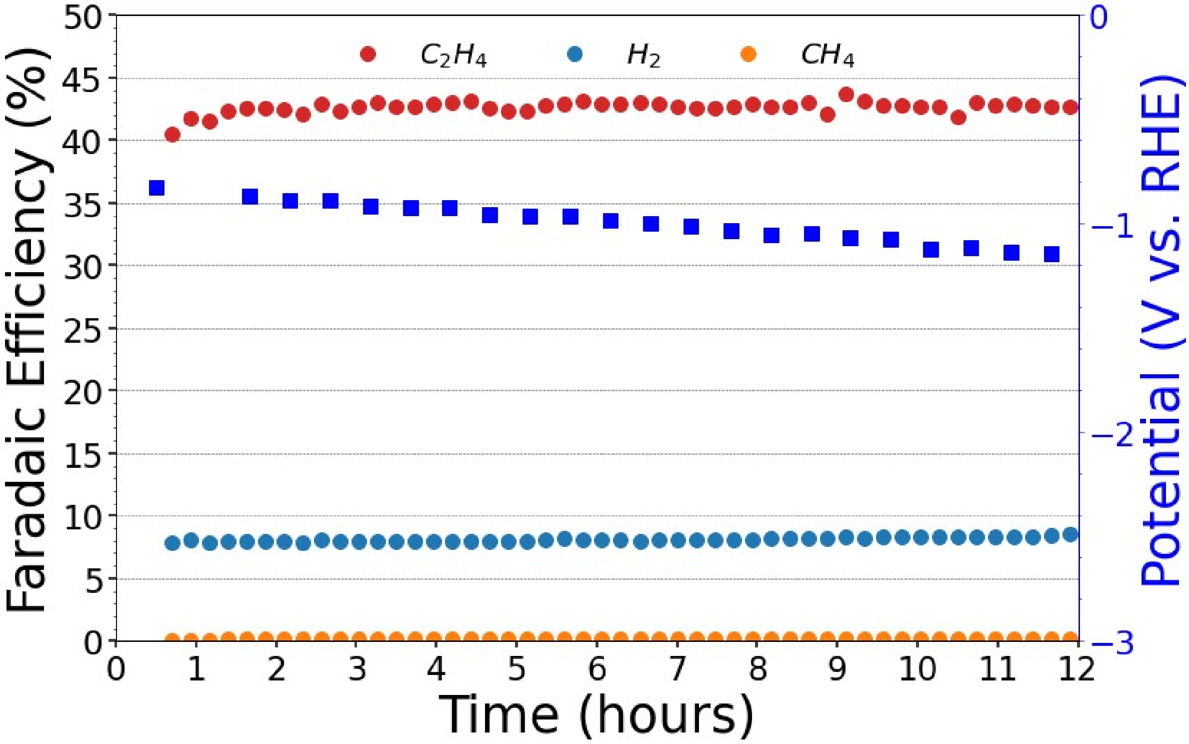

Fig. S14. Stability of DRY/20%PTFE/30min for 12 h flow cell testing at 200 mA cm^{-2}.

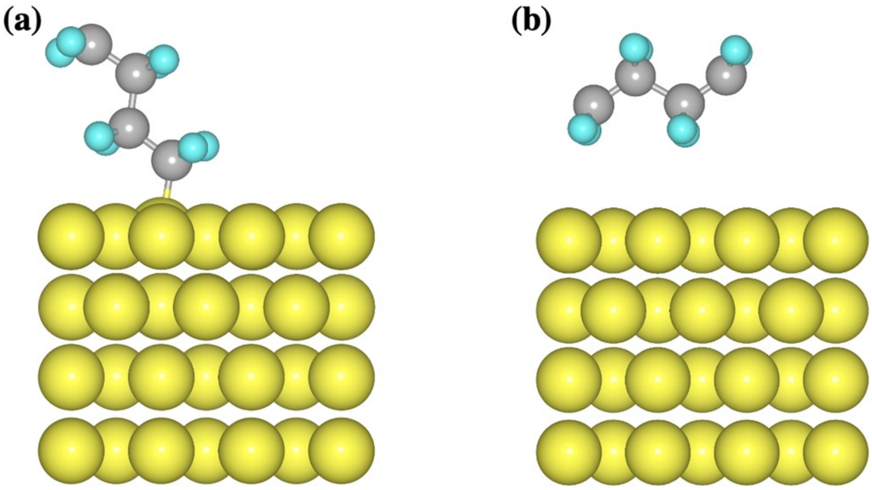

Fig. S15. Atomistic structures of a short $(CF_2)_4$ chain (a) chemically adsorbed perpendicularly and (b) physically adsorbed parallelly on a Cu(111) surface. In the Fig., the yellow, grey and cyan balls represent Cu, C, and F atoms, respectively.

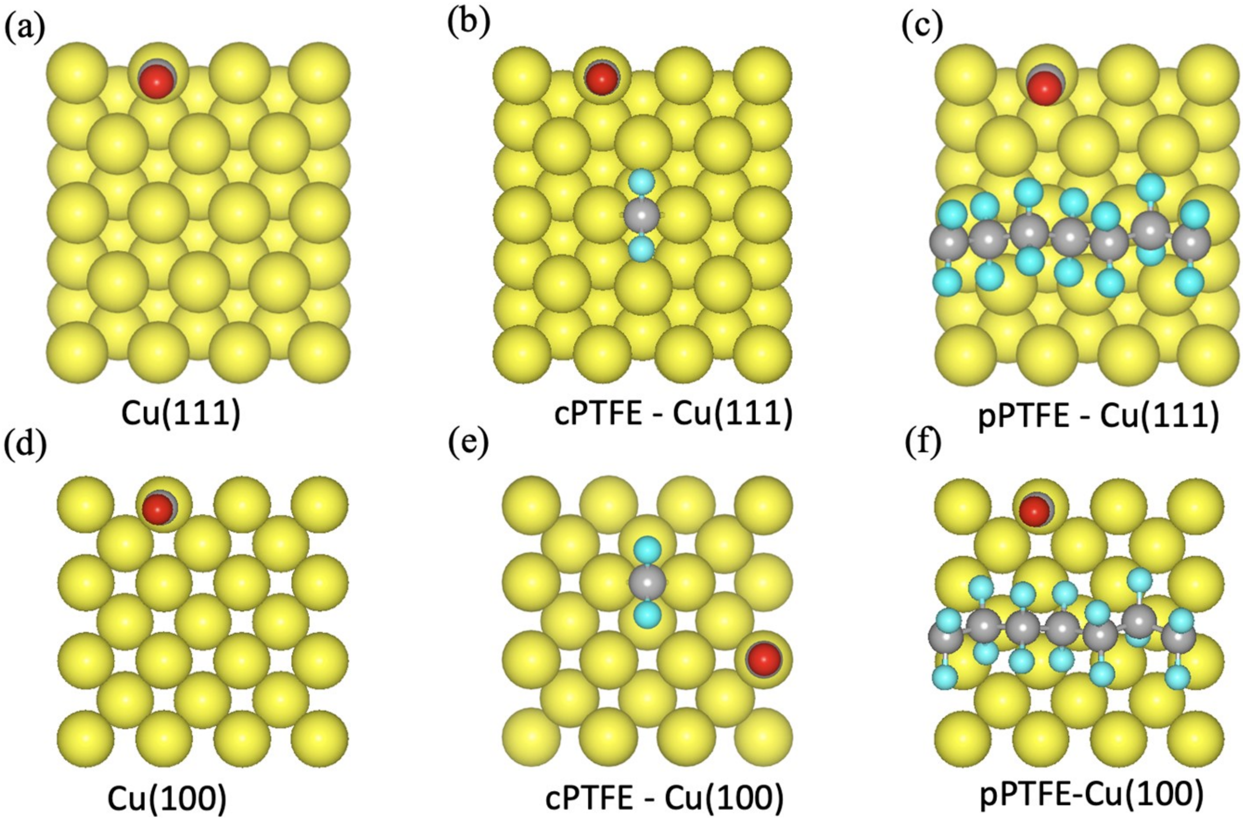

Fig. S16. Optimized configuration of CO adsorption on (a) clean Cu(111), (b) cPTFE- Cu(111), (c) pPTFE-Cu(111), (d) clean Cu(100), (e) cPTFE-Cu(100), and (f) pPTFE-Cu(100) surface. In the Fig., the yellow, grey, cyan, and red balls represent Cu, C, F, and O atoms, respectively. The Cu site covered by CO was chosen as the active site to catalyze CO_2 reduction.

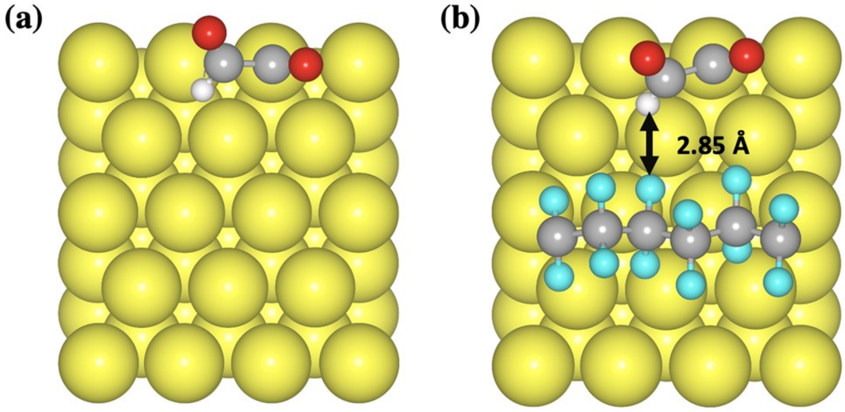

Fig. S17. Optimized adsorption configurations of *COCHO on (a) Cu(111), and (b) pPTFE-Cu(111) surfaces. Here, the yellow, grey, cyan, red, and white balls represent Cu, C, F, O, and H atoms, respectively.

Table S1. Water contact angle of as prepared cathodes.

Catalyst Deposited Onto GDL	**Contact Area ±2 (°)**
WET/20%PTFE	115
WET/20%Nafion	145
DRY/20%PTFE/0sec	Not able to deposit
DRY/20%PTFE/30sec	140
DRY/20%PTFE/60min	145
DRY/5%PTFE/30min	140
DRY/15%PTFE/30min	145
DRY/20%PTFE/30min	145
DRY/25%PTFE/30min	140
DRY/35%PTFE/30min	145

Table S2. Detected product concentration when a current density of 400 mA cm^{-2} is applied to a Cu and PTFE containing cathode under a gaseous feed of Ar.

	Product							
	H_2	**CO**	**CH_4**	**Formate**	**n-Propanol**	**Acetate**	**C_2H_5OH**	**C_2H_4**
Detected PPM	4600	0	2*	0	0	0	0	0

* When CO_2 is used as the feed gas detected ranges of CH_4 are around 30 ppm when tested at 400 mA cm^{-2}. Due to the low concentration and the lack of evidence of any other carbon products it is assumed that this detected CH_4 is a containment either from the Ar supply tank or the atmosphere.

Table S3. Detailed Faradaic efficiency of all the CO2RR products and potentials when catalyst prepared with differing PTFE mass loadings were tested under 200 mA cm^{-2}.

PTFE Mass Loading	**Faradaic Efficiency (%)**								**V (vs. RHE)**
	H_2	**CO**	**CH_4**	**C_2H_2**	**Formate**	**Ethanol**	**Acetate**	**n-propanol**	
5%	5.3 ± 0.1	47.8 ± 3.1	0.1 ± 0.1	24.2 ± 4.1	4.4 ± 0.6	10.5 ± 2.9	0.5 ± 0.2	3.7 ± 0.1	-0.86 ± 0.02
15%	6.5 ± 0.4	36.2 ± 5.8	0.0 ± 0.0	28.2 ± 0.4	5.6 ± 1.8	14.2 ± 1.5	0.6 ± 0.1	6.2 ± 1.5	-1.06 ± 0.16
20%	9.1 ± 0.2	14.4 ±0.8	0.1 ±0.0	43.2 ±0.8	2.2 ± 0.2	22.8 ± 0.5	0.9 ± 0.0	4.9 ± 0.2	-1.34 ± 0.01
25%	27.1 ± 5.5	6.5 ±2.3	2.2 ±1.1	33.5 ±4.4	1.1 ± 0.4	23.0 ± 0.6	2.7 ± 1.0	1.2 ± 1.2	-1.29 ± 0.06
35%	67.9 ± 0.6	3.2 ± 0.2	13.0 ± 1.4	3.8 ± 0.6	1.1 ± 0.2	9.0 ± 2.1	2.5 ± 0.4	0.0 ± 0.0	-1.53 ± 0.22

Table S4. Detailed Faradaic efficiency of all the CO2RR products and potentials of catalyst prepared with 20% PTFE mass loading, but various ball-milling times tested under 200 mA cm^{-2}.

Ball-milling Time	**Faradaic Efficiency (%)**								**V (vs. RHE)**
	H_2	**CO**	**CH_4**	**C_2H_2**	**Formate**	**Ethanol**	**Acetate**	**n-propanol**	
30 sec	7.1 ± 0.3	33.6 ± 1.4	0.1 ± 0.0	33.1 ± 0.2	4.0 ± 0.0	15.2 ± 0.4	0.8 ± 0.1	5.2 ± 0.2	-1.22 ± 0.17
9 min	7.3 ± 0.3	32.4 ± 1.8	0.0 ± 0.0	33.0 ± 1.1	5.6 ± 0.1	16.2 ± 0.4	0.5 ± 0.0	5.2 ± 1.8	-0.89 ± 0.00
15 min	7.7 ± 0.1	28.2 ± 0.3	0.0 ± 0.0	35.4 ± 0.3	4.8 ± 0.3	16.9 ± 0.4	0.5 ± 0.1	6.3 ± 0.0	-0.8 ± 0.01
30 min	9.1 ± 0.2	14.4 ± 0.8	0.1 ± 0.0	43.2 ± 0.8	2.2 ± 0.2	22.8 ± 0.5	0.9 ± 0.0	4.9 ± 0.2	-1.34 ± 0.01
60 min	10.5 ± 0.1	13.2 ± 2.2	0.2 ± 0.1	42.8 ± 2.3	2.2 ± 0.5	24.3 ± 1.7	1.0 ± 0.2	4.5 ± 0.6	-1.06 ± 0.01

Table S5. Detailed Faradaic efficiency of all the CO2RR products and potentials when testing DRY/20%PTFE/30min under various current densities.

Current Density (mA cm^{-2})	**Faradaic Efficiency (%)**								**V (vs. RHE)**
	H_2	**CO**	**CH_4**	**C_2H_2**	**Formate**	**Ethanol**	**Acetate**	**n-propanol**	
100	9.1 ± 0.1	29.6 ± 0.5	0.1 ± 0.1	26.6 ± 3.1	5.6 ± 1.7	19.1 ± 7.5	0.6 ± 0.2	5.2 ± 1.0	-1.00 ± 0.17
200	9.1 ± 0.2	14.4 ± 0.8	0.1 ± 0.0	43.2 ± 0.8	2.2 ± 0.2	22.8 ± 0.5	0.9 ± 0.0	4.9 ± 0.2	-1.34 ± 0.01
300	9.3 ± 0.6	12.4 ± 2.0	0.1 ± 0.0	44.7 ± 0.9	1.7 ± 0.1	23.7 ± 4.1	1.0 ± 0.3	4.3 ± 0.1	-1.67 ± 0.17
400	11.1 ± 0.9	8.3 ± 0.8	0.2 ± 0.1	44.3 ± 2.3	1.2 ± 0.2	28.4 ± 0.4	1.9 ± 0.3	3.1 ± 0.2	-1.87 ± 0.03
500	14.9 ± 0.9	4.6 ± 1.2	0.2 ± 0.0	37.9 ± 4.0	1.1 ± 0.3	31.4 ± 4.8	3.4 ± 1.1	2.8 ± 0.5	-1.99 ± 0.37
600	25.9 ± 3.9	4.0 ± 0.9	0.6 ± 0.3	35.7 ± 2.7	0.6 ± 0.1	27.1 ± 1.6	3.7 ± 0.7	1.7 ± 0.6	-2.44 ± 0.25
700	33.2 ± 2.6	3.5 ± 0.7	0.8 ± 0.3	31.5 ± 2.5	0.6 ± 0.1	25.0 ± 1.3	3.5 ± 0.5	1.5 ± 0.4	-2.86 ± 0.10

Table S6. Detailed Faradaic efficiency of all the CO2RR products and potentials when testing WET/20%PTFE under various current densities.

Current Density (mA cm^{-2})	**Faradaic Efficiency (%)**								**V (vs. RHE)**
	H_2	**CO**	**CH_4**	**C_2H_2**	**Formate**	**Ethanol**	**Acetate**	**n-propanol**	
100	15.7 ± 0.0	51.6 ± 2.3	0.0 ± 0.0	11.6 ± 1.4	10.4 ± 0.4	6.8 ± 1.2	0.5 ± 0.2	2.6 ± 0.7	-0.66 ± 0.01
200	19.3 ± 3.7	30.8 ± 2.6	0.3 ± 0.2	21.7 ± 0.8	7.8 ± 0.3	12.7 ± 3.1	0.8 ± 0.2	4.5 ± 0.8	-0.80 ± 0.11
300	17.6 ± 3.8	23.7 ± 0.9	0.3 ± 0.1	32.1 ± 4.4	6.6 ± 0.3	11.9 ± 1.1	0.7 ± 0.1	5.0 ± 0.8	-1.04 ± 0.12
400	14.3 ± 2.8	21.7 ± 2.7	0.1 ± 0.0	34.4 ± 0.4	5.5 ± 0.6	14.8 ± 3.0	0.8 ± 0.2	5.8 ± 0.8	-1.11 ± 0.08
500	15.7 ± 2.8	20.9 ± 0.7	0.1 ± 0.0	38.2 ± 1.2	4.7 ± 0.8	12.0 ± 0.5	0.6 ± 0.1	4.9 ± 0.4	-1.29 ± 0.11
600	16.4 ± 2.4	17.1 ± 0.6	0.3 ± 0.1	39.5 ± 1.6	3.7 ± 0.5	16.0 ± 0.7	1.0 ± 0.0	5.0 ± 0.2	-1.41 ± 0.06
700	16.5 ± 1.5	15.6 ± 1.4	0.2 ± 0.1	43.4 ± 1.0	2.8 ± 0.2	14.9 ± 0.8	0.9 ± 0.1	5.2 ± 0.3	-1.56 ± 0.06

Table S7. Detailed Faradaic efficiency of all the CO2RR products and potentials when testing WET/20%Nafion under various current densities.

Current Density (mA cm^{-2})	**Faradaic Efficiency (%)**								**V (vs. RHE)**
	H_2	**CO**	**CH_4**	**C_2H_2**	**Formate**	**Ethanol**	**Acetate**	**n-propanol**	
100	22 ± 5.2	34.4 ±12.2	0.1 ± 0.1	12.7 ± 1.6	15.2 ± 0.5	10.4 ± 4.4	0.6 ± 0.2	4.4 ± 1.0	-0.62 ± 0.01
200	24.5 ± 2.3	28.6 ± 1.5	0.5 ± 0.1	17.8 ± 2.4	10.5 ± 0.5	13.3 ± 2.2	0.5 ± 0.1	3.7 ± 0.1	-0.83 ± 0.07
300	20.9 ± 3.1	22.1 ± 4.3	0.4 ± 0.2	27.9 ± 7.4	8.0 ± 0.8	15.7 ± 1.4	0.4 ± 0.0	4.7 ± 0.3	-0.96 ± 0.10
400	21.2 ± 2.1	22.8 ± 0.6	2.1 ± 0.4	23.6 ± 1.1	5.4 ± 0.1	19.3 ± 2.9	0.7 ± 0.0	3.9 ± 0.6	-1.32 ± 0.20
500	19.5 ± 0.3	22.8 ±0.4	4.5 ± 0.3	24.5 ± 0.7	3.0 ± 0.2	21.1 ± 0.1	1.7 ± 0.2	2.7 ± 0.2	-1.54 ± 0.15
600	23.5 ± 1.5	20.9 ± 3.1	3.1 ± 2.9	26.5 ± 0.7	4.5 ± 1.9	16.1 ± 4.5	1.3 ± 0.8	3.9 ± 1.2	-1.71 ± 0.24
700	28.5 ± 3.1	12.7 ± 5.2	3.1 ±3.0	27.9 ± 4.7	3.1 ± 1.7	16.3 ± 2.7	1.5 ± 0.9	3.7 ± 2.1	-2.18 ± 0.78

Table S8. A summary of recent representative catalysts for CO2-to-ethylene and ethanol conversion.

Catalyst	**Electrolyte**	**FE(C_{2+}) (%)**	**Approx. C_{2+}/C_1 Product Ratio**	**Current density (mA cm^{-2})**	**CO_2 Flow Rate**	**Active area (cm^2)**	**Ref**
PTFE Coated Cu Nanoparticles	1 M KOH	77.6	8.1	400	30 ml	1	This work
PTFE Coated Cu Nanoparticles	1 M KOH	75.5	12.9	500	30 ml	1	This work
Cu/C/PTFE	1 M KOH	~52	3.4	~250	5 sccm	0.66	[16] Nat. Commun. 2021
Ce(OH)x/Cu/PTFE	1 M KOH	~78	0.7	128	50 sccm	1	[17] Nat. Commun. 2019
graphite/carbon NPs/Cu/PTFE	10 M KOH	~85	11.5	225	30 mL	Not reported	[18] Science 2018
de-alloyed Cu-Al	1 M KOH	>80	No liquid products reported	400	56 sccm	1	[19] Nat. 2020
Cu nanosheets with nanoscaled defects (H-cell testing)	0.1M K_2SO_4	83.2	No C_1 products reported	~60	Not reported	0.07	[20] J. Am. Chem. Soc. 2020
CuO/Al2CuO4-23 (H-cell testing)	0.1 M KHCO3	82.4	38.5	Not reported	Not reported	Not reported	[21] Energy Environ. Sci. 2022
CuO/Al2CuO4-23	1 M KOH	70.1	5.4	600	20 sccm	1	[21] Energy Environ. Sci. 2022
N-Doped C/Cu	1 M KOH	93	29.2	~300	50 mL	5	[22] Nat. Energy 2020
N-doped graphene quantum dots on oxide-derive Cu nanorods	1 M KOH	75	6.9	282	20 sccm	1	[23] Angew. Chem., Int. Ed. 2020
Ag0.14/Cu0.86	1 M KOH	~56	1.84	400	Not reported	Not reported	[24] J. Am. Chem. Soc. 2019
Pyridinium/Cu	1 M KHCO3	86	13.8	232	50 sccm	1	[25] Nature 2020
In situ electrodeposited Cu	7 M KOH	90	17.8	580	50 sccm	1	[26] Nat. Cal. 2020
Catalyst:ionomer bulk heterojunction	7 M KOH	67.2	3.7	510	50 mL	1	[27] Science 2020
Catalyst:ionomer bulk heterojunction	7 M KOH	87.5	8.2	1170	50 mL	1	[27] Science 2020

Table S9. Calculated CO adsorption energy, free energy change of CO-CO dimerization, and free energy change of CO-CHO dimerization on different Cu surfaces.

	Cu(111)	**CF2-Cu(111)**	**PTFE-Cu(111)**	**Cu(100)**	**CF2-Cu(100)**	**PTFE-Cu(100)**
CO adsorption energy (eV)	-0.47	-0.48	-0.51	-0.54	-0.55	-0.59
Free energy change of CO-CO (eV)	1.32	1.30	1.13	0.73	0.71	0.68
Free energy change of CO-CHO (eV)	-0.24	-0.24	-0.29	-0.31	-0.31	-0.38
Activation energy for CO-CHO (eV)	0.83	0.82	0.78	0.65	0.64	0.60

Table S10. Calculated number of electrons per Cu atom on intrinsic and PTFE decorated Cu(111) surface.

Model	**Intrinsic Cu(111)**	**pPTFE-Cu(111)**
Number of electrons per Cu atom	11.000	10.996

References:

1. T. Zheng, K. Jiang, N. Ta, Y. Hu, J. Zeng, J. Liu and H. Wang, *Joule*, 2019, **3**, 265-278.
2. Z. Gu, H. Shen, Z. Chen, Y. Yang, C. Yang, Y. Ji, Y. Wang, C. Zhu, J. Liu, J. Li, T.-K. Sham, X. Xu and G. Zheng, *Joule*, 2021, **5**, 429-440.
3. X. Chen, J. Chen, N. M. Alghoraibi, D. A. Henckel, R. Zhang, U. O. Nwabara, K. E. Madsen, P. J. A. Kenis, S. C. Zimmerman and A. A. Gewirth, *Nat Catal*, 2021, **4**, 20-27.
4. N. C. Buggy, I. Wu, Y. Du, R. Ghosh, M.-C. Kuo, M. S. Ezell, J. M. Crawford, S. Seifert, M. A. Carreon, E. B. Coughlin and A. M. Herring, *Electrochim Acta*, 2022, **412**, 140124.
5. A. Lindner, H. Radinger, F. Scheiba and H. Ehrenberg, *RSC Adv.*, 2022, **12**, 14119-14126.
6. P. Hohenberg and W. Kohn, *Physical Review*, 1964, **136**, B864-B871.
7. W. Kohn and L. J. Sham, *Physical Review*, 1965, **140**, A1133-A1138.
8. G. Kresse and J. Hafner, *Physical Review B*, 1993, **47**, 558-561.
9. G. Kresse and J. Furthmuller, *Comp Mater Sci*, 1996, **6**, 15-50.
10. P. E. Blochl, *Physical Review B*, 1994, **50**, 17953-17979.
11. G. Kresse and D. Joubert, *Physical Review B*, 1999, **59**, 1758-1775.
12. B. Hammer, L. B. Hansen and J. K. Nørskov, *Phys. Rev. B*, 1999, **59**, 7413-7421.
13. H. J. Monkhorst and J. D. Pack, *Physical Review B*, 1976, **13**, 5188-5192.
14. B. Hagman, A. Posada-Borbón, A. Schaefer, M. Shipilin, C. Zhang, L. R. Merte, A. Hellman, E. Lundgren, H. Grönbeck and J. Gustafson, *J. Am. Chem. Soc.*, 2018, **140**, 12974-12979.
15. Y. Y. Birdja, E. Pérez-Gallent, M. C. Figueiredo, A. J. Göttle, F. Calle-Vallejo and M. T. Koper, *Nature Energy*, 2019, **4**, 732-745.
16. Z. Xing, L. Hu, D. S. Ripatti, X. Hu and X. Feng, *Nature Communications*, 2021, **12**, 136.
17. M. Luo, Z. Wang, Y. C. Li, J. Li, F. Li, Y. Lum, D.-H. Nam, B. Chen, J. Wicks, A. Xu, T. Zhuang, W. R. Leow, X. Wang, C.-T. Dinh, Y. Wang, Y. Wang, D. Sinton and E. H. Sargent, *Nat Commun*, 2019, **10**, 5814.
18. C.-T. Dinh, T. Burdyny, M. G. Kibria, A. Seifitokaldani, C. M. Gabardo, F. P. García de Arquer, A. Kiani, J. P. Edwards, P. De Luna, O. S. Bushuyev, C. Zou, R. Quintero-Bermudez, Y. Pang, D. Sinton and E. H. Sargent, *Science*, 2018, **360**, 783-787.
19. M. Zhong, K. Tran, Y. Min, C. Wang, Z. Wang, C.-T. Dinh, P. De Luna, Z. Yu, A. S. Rasouli, P. Brodersen, S. Sun, O. Voznyy, C.-S. Tan, M. Askerka, F. Che, M. Liu, A. Seifitokaldani, Y. Pang, S.-C. Lo, A. Ip, Z. Ulissi and E. H. Sargent, *Nature*, 2020, **581**, 178-183.
20. B. Zhang, J. Zhang, M. Hua, Q. Wan, Z. Su, X. Tan, L. Liu, F. Zhang, G. Chen, D. Tan, X. Cheng, B. Han, L. Zheng and G. Mo, *Journal of the American Chemical Society*, 2020, **142**, 13606-13613.
21. S. Sultan, H. Lee, S. Park, M. M. Kim, A. Yoon, H. Choi, T.-H. Kong, Y.-J. Koe, H.-S. Oh, Z. Lee, H. Kim, W. Kim and Y. Kwon, *Energy & Environmental Science*, 2022, **15**, 2397-2409.
22. X. Wang, Z. Wang, F. P. García de Arquer, C.-T. Dinh, A. Ozden, Y. C. Li, D.-H. Nam, J. Li, Y.-S. Liu, J. Wicks, Z. Chen, M. Chi, B. Chen, Y. Wang, J. Tam, J. Y. Howe, A. Proppe, P. Todorović, F. Li, T.-T. Zhuang, C. M. Gabardo, A. R. Kirmani, C. McCallum, S.-F. Hung, Y. Lum, M. Luo, Y. Min, A. Xu, C. P. O'Brien, B. Stephen, B. Sun, A. H. Ip, L. J. Richter, S. O. Kelley, D. Sinton and E. H. Sargent, *Nature Energy*, 2020, **5**, 478-486.
23. C. Chen, X. Yan, S. Liu, Y. Wu, Q. Wan, X. Sun, Q. Zhu, H. Liu, J. Ma, L. Zheng, H. Wu and B. Han, *Angew Chem Int Ed*, 2020, **59**, 16459-16464.
24. Y. C. Li, Z. Wang, T. Yuan, D.-H. Nam, M. Luo, J. Wicks, B. Chen, J. Li, F. Li, F. P. G. de Arquer, Y. Wang, C.-T. Dinh, O. Voznyy, D. Sinton and E. H. Sargent, *Journal of the American Chemical Society*, 2019, **141**, 8584-8591.
25. F. Li, A. Thevenon, A. Rosas-Hernández, Z. Wang, Y. Li, C. M. Gabardo, A. Ozden, C. T. Dinh, J. Li, Y. Wang, J. P. Edwards, Y. Xu, C. McCallum, L. Tao, Z.-Q. Liang, M. Luo, X. Wang, H. Li, C. P. O'Brien, C.-S. Tan, D.-H. Nam, R. Quintero-Bermudez, T.-T. Zhuang, Y. C. Li, Z. Han, R. D. Britt, D. Sinton, T. Agapie, J. C. Peters and E. H. Sargent, *Nature*, 2020, **577**, 509-513.

26. Y. Wang, Z. Wang, C.-T. Dinh, J. Li, A. Ozden, M. Golam Kibria, A. Seifitokaldani, C.-S. Tan, C. M. Gabardo, M. Luo, H. Zhou, F. Li, Y. Lum, C. McCallum, Y. Xu, M. Liu, A. Proppe, A. Johnston, P. Todorovic, T.-T. Zhuang, D. Sinton, S. O. Kelley and E. H. Sargent, *Nat Catal*, 2020, **3**, 98-106.
27. F. P. García de Arquer, C.-T. Dinh, A. Ozden, J. Wicks, C. McCallum, A. R. Kirmani, D.-H. Nam, C. Gabardo, A. Seifitokaldani, X. Wang, Y. C. Li, F. Li, J. Edwards, L. J. Richter, S. J. Thorpe, D. Sinton and E. H. Sargent, *Science*, 2020, **367**, 661-666.